## ARTICLE

OPEN

Check for updates

Ultrafast dynamics of exchange stiffness in Co/Pt multilayer

Je-Ho Shim[1,2,8], Akbar Ali Syed[1,2,8], Yooleemi Shin[2,3], Ji-Wan Kim[2,3], Hong-Guang Piao[4,5], Sang-Hyuk Lee[4,6], Kyung Min Lee[7], Jong-Ryul Jeong [7], Dong-Hyun Kim[4✉] & Dong Eon Kim[1,2✉]

The exchange stiffness coefficient, A_{ex}, represents the strength of direct exchange interactions among neighboring spins. A_{ex} is linked to most of the magnetic properties such as skyrmion formation, magnetic vortex, magnetic domain wall width, and exchange length. Hence, the quantification of A_{ex} is essential to understanding fundamental magnetic properties, but little is known for the dynamics of A_{ex} on a sub-picosecond timescale. We report the ultrafast dynamcis of A_{ex} in an ordered magnetic state in Co/Pt ferromagnetic multilayer. Time-resolved magneto-optical Kerr effect and reflectivity measurements were analyzed for various pump fluences. We reveal that the significant dynamical reduction of A_{ex} is responsible for the dramatic increase of remagnetization time for high fluences. The analysis shows that A_{ex} dynamically varies, strongly affecting overall ultrafast demagnetization/ remagnetization process. The investigation demonstrates the possibility of A_{ex} engineering in femtosecond timescale and thereby provides a way to design ultrafast spintronic devices.

[1] Department of Physics and Center for Attosecond Science and Technology, POSTECHPohang 37673, South Korea. [2] Max Planck POSTECH/KOREA Research Initiative, Pohang 37673, South Korea. [3] Department of Physics, Kunsan National University, Kunsan 54150, South Korea. [4] Department of Physics, Chungbuk National University, Cheongju 28644, South Korea. [5] College of Science, China Three Gorges University, 443002 Yichang, P. R. China. [6] Division of Industrial Metrology, Korea Research Institute of Standards and Science (KRISS), Daejeon 34113, South Korea. [7] Department of Material Science and Engineering and Graduate School of Energy Science and Technology, Chungnam National University, Daejeon 34134, South Korea. [8] These authors contributed equally: Je-Ho Shim, Akbar Ali Syed. ✉email: donghyun@cbnu.ac.kr; kimd@postech.ac.kr

The exchange interaction is a fundamental aspect of ferromagnetism[1–3]; this interaction, underpinning the existence of ordered magnetic states, allows the alignment of neighboring spins in a system. The origin of the direct exchange interaction is ascribed to the overlapping of electron wave functions among neighboring atoms with no classical analogy, and its strength depends sensitively on the atomic and lattice structure[4,5], while there also exist other exchange mechanisms such as Dzyaloshinskii-Moriya interaction[6,7], and superexchange interaction[8]. The strength of the direct exchange interaction is represented by the exchange-stiffness coefficient A_{ex}, which is a material parameter mostly depending on the atomic and lattice structure and detailed characteristics of which are determined by the electronic band structure[9–11]. Fundamental mechanisms of novel spin phenomena, such as magnetic vortices[12,13] and skyrmions[14,15], might be understood based on a quantitative analysis of A_{ex}. It has been known that A_{ex} is temperature-dependent[16,17]. As the temperature increases, thermal agitation reduces the degree of the ordering of neighboring spins, effectively lowering the value of A_{ex}.

Although the temperature-dependence of A_{ex} is relatively well recognized in static cases[17], very little is known regarding how A_{ex} varies on an in the ultrafast timescale. In case of ultrafast photo-induced demagnetization, as the fluence F_P of a pump laser increases, the disorder in a spin system should increase so that the effective spin temperature should also increase. It is then expected that the remagnetization time of the system from an excited disordered state to a stable equilibrium state should increase as F_P increases. Recent reports of the dynamics of the exchange interaction on ultrafast timescale have shown that a fundamental exchange interaction varies on scales of several tens of femtoseconds in ferromagnetic NiFe alloy[18] and antiferromagnetic $KNiF_3$[19]. A possibility of ultrafast control of exchange interaction by using a femtosecond pump laser has been proposed theoretically[20–22]. All of these results indicate that the exchange interaction or exchange splitting dramatically changes by a femtosecond pump laser. However, to our best knowledge, no systematic study has been conducted to quantify the dynamics of A_{ex} on ultrafast timescale.

Here, we report, the dynamics of A_{ex} on a femtosecond timescale in Co/Pt multilayers for a range of F_P, demonstrating that A_{ex} varies rapidly, affecting spin dynamics and its variation can be controlled by the pump fluence. While the electron-spin interaction strength is kept constant all the time in the conventional three-temperature model (3TM) in the study of ultrafast magnetism, the dynamic change of A_{ex} is considered, adopting the generalized three-temperature model (G-3TM) developed by A. Manchon et al[23].

Results

Fluence dependent remagnetization time
We performed time-resolved magneto-optical Kerr effect (TR-MOKE) measurements for [Co (6.2 Å)/Pt (7.7 Å)]$_5$ multilayer film, of which the magnetic properties such as perpendicular magnetic anisotropy and saturation magnetization are well known[7,24–27]. A detailed experimental configuration was reported elsewhere[28]. TR-MOKE signals were measured for $1.7 \leq F_P \leq 28.5$ mJ cm^{-2} for time delays of up to 30 ps. To exclude the dichroic bleaching effect, the experiments are carried out by pump beam at both 400 and 800 nm wavelength (λ_{pump}). TR-MOKE vs. time at different fluences is plotted in Fig. 1a for the case of $\lambda_{pump} = 800$ nm, while no significant difference is observed in the overall trend for the case of $\lambda_{pump} = 400$ nm. The signals were normalized by their maximum changes to compare the dynamical behaviors in remagnetization for different conditions. An external magnetic
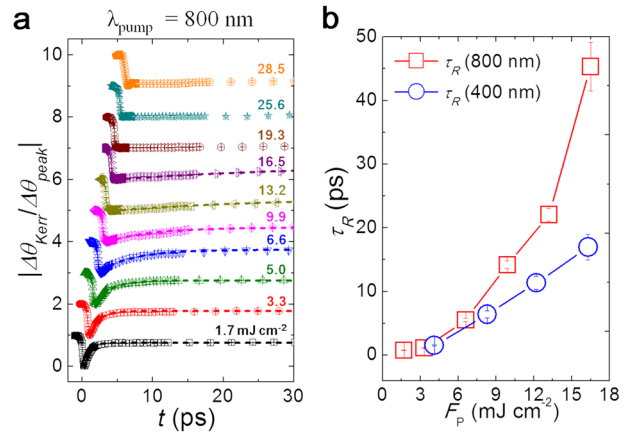
Fig. 1 Temporal change of induced magnetization with respect to pump fluence F_P. a Time-resolved magneto-optical Kerr effect signal (open symbols) with single exponential fitting curves (dashed lines) for wavelength of pump pulse $\lambda_{pump} = 800$ nm. The values of F_P pump fluence are written next to the experimental data. The data have shifted upwards for easy recognition. Error bars represent standard error of the avaraged raw data. **b** Remagnetization time τ_R with respect to fluence for $\lambda_{pump} = 800$ nm (square) and $\lambda_{pump} = 800$ nm (circle). Error bars represent standard error of the single exponential fitting.

field of 1.7 kOe was applied normally to the film surface. All the measured curves exhibit clearly the dynamics of photo-induced demagnetization and subsequent remagnetization. The maximal change of demagnetization is observed around $t = 0.3$ ps for all the fluence cases. In case of $\lambda_{pump} = 800$ nm, as F_P was increased from 1.7 to 28.5 mJ cm^{-2}, the remagnetization was slowed down for $F_P > 9.9$ mJ cm^{-2}. The remagnetization behavior at $1.7 \leq F_P \leq 16.5$ mJ cm^{-2} well-fitted with a single exponential curve (Fig. 1a, dotted lines), yielding the characteristic time τ_R of remagnetization (open square in Fig. 1b). We note that τ_R increased drastically as F_P increased by only a factor of a few. Fitting with a single exponential curve was not valid for $F_P > 16.5$ mJ cm^{-2}. A similar trend is observed for the case of $\lambda_{pump} = 400$ nm, where τ_R is fitted with a single exponential curve as well.

G-3TM analysis. For further understanding, we conducted G-3TM analysis for the TR-MOKE data[23,28,29]. G-3TM is composed of three coupled equations (see Supplementary Note 1 for more details):

$$C_e(T_e)\frac{dT_e}{dt} = -G_{el} \times (T_e - T_l) - G_{es}[T_e, T_s] \times (T_e - T_s) + P(t)$$

$$C_l(T_l)\frac{dT_l}{dt} = -G_{el} \times (T_l - T_e) - G_{ls} \times (T_l - T_s) - K_l \times (T_l - 300)^3$$

$$C_s(T_s)\frac{dT_s}{dt} = -G_{es}[T_e, T_s] \times (T_s - T_e) - G_{ls} \times (T_s - T_l)$$

$$(1)$$

where T_e, T_l, and T_s are the electron, lattice, and spin temperatures, respectively. C_e, C_l, and C_s are the specific heats of the electron, lattice, and spin, respectively. G_{el}, G_{es}, and G_{ls} are the electron-lattice, electron-spin, and lattice-spin interaction channels, respectively. $P(t)$ is a laser source term with a Gaussian temporal profile. The term that contains K_l represents lattice thermal diffusion, which is modeled to be proportional to the third power of the temperature increase of lattice system[30]. A typical relation between the magnetization and the spin temperature: $\propto (1 - (T_s / T_C))^{0.5}$, where T_C is Curie temperature of 1131 K[17], to match the normalized TR-MOKE signal ($|\Delta\theta_{Kerr}|/|\Delta\theta_{peak}|$).

In conventional 3TM, G_{el}, G_{es}, and G_{ls} have been set to be constant over time. However, in our study, for correct analysis, the electron-spin interaction channel(G_{es}) was allowed to change over time. Adopting the G-3TM, G_{es} can be written as

$$G_{es}[T_e, T_s] = G_{es0} \frac{(M[T_s])^3 \left(G_2\left[\frac{T_e}{DT_C}\right] - G_2\left[\frac{T_s}{DT_C}\right]\right)}{T_e - T_s}, \quad (2)$$

$$\text{where } G_2[x] = x^3 \int_0^{1/x} \frac{t^2}{e^t - 1} dt, \text{ and} \quad (3)$$

$$G_{es0} = (6\pi^2)^{10/3} \frac{(2aA_{ex0})^2 S^3}{2\hbar V} \left(\frac{T_C}{T_F}\right)^2, \quad (4)$$

where a is a lattice constant, A_{ex0} an exchange-stiffness coefficient at 0 K, V unit cell volume, T_F Fermi temperature, $S = 3/2$ spin quantum number, M magnetization and G_2 a function based on the second-order Debye function[23] (Eq. (3)). T_F is Fermi temperature, chosen to be that of fcc Co ($T_F = 16.87 Ry/k_B$)[31]. $D = S M[T_s] q_m^2 a^2$, where q_m is magnon wave number $q_m = k_F = (6\pi^2)^{1/3}a^{-1}$, and k_F is Fermi wave number. Features of $G_e[T_e, T_s]$ is described in detail in Supplementary Note 1. G_{es0} (Eq. (4)) is a temperature-independent electron-spin interaction channel. In static case, it is well known that $A_{ex} \propto (J_{ex} a^{-1}) <S^2>$, where J_{ex} is an exchange interaction constant, a is a lattice constant. The proportionality depends on material parameters such as a periodic lattice configuration. Since A_{ex} can be easily measured rather than J_{ex}, we focus on qauntifying A_{ex} on an ultrafast timescale. When the relation between A_{ex} and J_{ex} is extended, we have put $A_{ex}(T) \propto A_{ex0} <M(T)^2> \propto (J_{ex} a^{-1}) <S(T)^2>$, where the temperature T dependence is included in $<M(T)^2>$ without affecting J_{ex}. For simplicity, we have used the approximation, $J_{ex} \sim 2aA_{ex0}$[16]. In the G-3TM, G_{el} is still assumed to be constant because the relaxation rate between the electron and the lattice is expected to be simply proportional to the temperature difference. G_{ls} was also set to be constant throughout the simulations.

The G-3TM is composed of several free parameters, so the fitting should be processed with care. First, time-resolved reflectivity $R(t)$ data were utilized to estimate values for C_e, C_l, and G_{el}, considering only the electron and lattice, based on the 2-temperature model[32,33]. In the full analysis using the G-3TM, the reflectivity and MOKE data were fitted. As a constraint in the analysis, the measured values for the degree of demagnetization (D_{demag}) were used (Fig. 2a, d). Hysteresis loop measurement is the best way to estimate the D_{demag}. The hysteresis loops were measured at $t = -2$ ps and 0.3 ps (the maximal demagnetization) using the same TR-MOKE setup with probe-beam modulation for all the F_P (Methods section). An example of measurements for $F_P = 13.2$ mJ cm^{-2} (Fig. 2a, inset) shows that a D_{demag} is 70%. The excellent match has been established in all the cases (See Supplementary Note 2, where the utilization of $R(t)$ measurement and the D_{demag} for fitting is described).

The G-3TM fitting determines temporal evolutions of spin, electron, and lattice temperature at wavelength of pump pulse $\lambda_{pump} = 800$ nm (Fig. 2b, c) and $\lambda_{pump} = 400$ nm (Fig. 2e, f). The cases for very high F_P corresponding to T_s being very close to Curie temperature (1131 K) are not considered, where the G-3TM may not be valid. The fitted value of C_e was $1.8 \sim 2.1 \times 10^3$ J (m^3 K^2)$^{-1}$ and, C_l was $1.8 \sim 5.0 \times 10^6$ J (m^3 K)$^{-1}$ [34,35] (all the fitting parameters are summarized in Supplementary Note 2). C_s should depend on the spin temperature T_s. In the original Manchon's paper[23] which the G-3TM on, C_s is determined from the numerical derivative of the spin energy. In fitting our data, we have found that the fitting becomes quite good if C_s is smaller than $\sim 10^4$ J (m^{3}K)$^{-1}$ in all cases. Thus, we used a small value of $C_s = 100$ J (m^{3}K)$^{-1}$ for all cases. The upper limit of fitted C_s value

($\sim 10^4$ J (m^{3}K)$^{-1}$) in the present work seems to be a little bit smaller than the reported values determined from 3TM. For instance, in Ref. [35], C_s of Ni and FeCuPt are 0.2×10^6 J (m^3 K)$^{-1}$ and 0.17×10^6 J (m^3 K)$^{-1}$.

The maximum values of electron temperature T_e^{max} and spin temperature T_s^{max} at $t = 0.3$ ps increased as F_P increased; e.g., T_s^{max} at $t = 0.3$ ps changes from 564 to 1040 K as F_P increases from 1.7 to 9.9 mJ cm^{-2} ($\lambda_{pump} = 800$ nm). High F_P increases the amount of energy transferred to the subsystems, so the increase of T_e^{max} and T_s^{max} is expected. The equilibrium temperature at which $T_e = T_l = T_s$ also increased consistently as F_P increased, but it is very interesting to note that the difference between T_e^{max} and T_s^{max} got larger substantially as F_P increased (Fig. 2b, c, Fig. 2e, f). In the context of the G-3TM, this observation indicates that the interaction channel G_{es} between the electron and spin subsystem is reduced, resulting in the increase of the thermal separation of the spin system from the electron subsystem as well as thereby the increase of the time required to reach thermal equilibrium. This phenomenon may be a reason for the increase of τ_R as F_P increases as observed in Fig. 1b.

Figure 3a is the plot of G_{es} (Eq. (4)) as a function of T_e and T_s. As T_s increases, G_{es} increases then decreases for a given electron temperature. The values T_e, T_s, and G_{es} determined from fitting to our experimental data at $\lambda_{pump} = 800$ nm are shown in a gray curved line in Fig. 3a, and again in Fig. 3b for various F_P. The case of $T_s = T_e$ is also presented as a dotted curve for guidance in Fig. 3b. The non-monotonic nature of G_{es} with respect to T_s is a direct consequence of Eq. (3). G_{es} increased monotonically with an increase in T_s at low $F_P = 1.7$ and 3.3 mJ cm^{-2}, but the increasing-then-decreasing behavior is observed at high $F_P > 6.6$ mJ cm^{-2}. We suspect that diverse experimental results of ultrafast demagnetization dynamics might be originated from this different trend of G_{es} at high F_P[36–38].

The dynamical variation of G_{es} on a femtosecond timescale is plotted for various F_P in Fig. 3c. At low F_P, the simple increase-and-decrease behavior of G_{es} is observed, with a maximum at $t = 0.3$ ps. The time of the maximum G_{es} coincides with the time at which the D_{demag} is the greatest. At high F_P, G_{es} quickly reaches the first peak right after the arrival of a pump pulse, decreased to a minimum at around the time of maximal D_{demag} ($t = 0.3$ ps), and then increased again. A comparison between the behaviors of G_{es}, G_{ls}, and G_{el} at $t = 0.3$ ps under various F_P (Fig. 3d) reveals that G_{el} is the strongest channel, G_{es} increased at low F_P, but decreases at high F_P; this trend may be the result from the feature of G_{es} (Fig. 3a, b). On the other hand, G_{ls} is the weakest channel (as often neglected) but becomes comparable to G_{es} as F_P increases. G_{ls} is involved with spin-orbit coupling[23], which might get stronger as T_e or D_{demag} [39].

The above discussion indicates that the dynamics of the photo-induced demagnetization and remagnetization in Co/Pt spin system is mostly governed by G_{es} and G_{ls}. Figure 3e shows a ratio of G_{es} to G_{ls} at $t = 0.3$ ps for various fluences. G_{es}/G_{ls} is larger than 10 for $F_P < 6.6$ mJ cm^{-2} for $\lambda_{pump} = 800$ and 400 nm. This imbalance implies that the spin-electron interaction is dominant in this F_P regime. For $F_P \geq 6.6$ mJ cm^{-2}, G_{es}/G_{ls} approaches unity asymptotically, indicating that spin-lattice interaction becomes increasingly important. The G-3TM fitting yields the values for G_{es}. Equations (2) and (4) allow us to calculate A_{ex0}, temperature-independent exchange-stiffness coefficient. The estimated value of A_{ex0} turns out to be 10.01 pJ m^{-1} at all the F_P; this value agrees well with a reported value for a Co/Pt multilayer[40,41]. Other analysis methods[42,43] could also reproduce the slow rate of magnetization at high fluences. It should be commented that the G-3TM based on the Hamiltonian for laser-induced demagneti-zation[23] allows us to separately monitor time-dependent G_{es} and G_{ls} as well as their ratio G_{es}/G_{ls}. In this work, we note that the
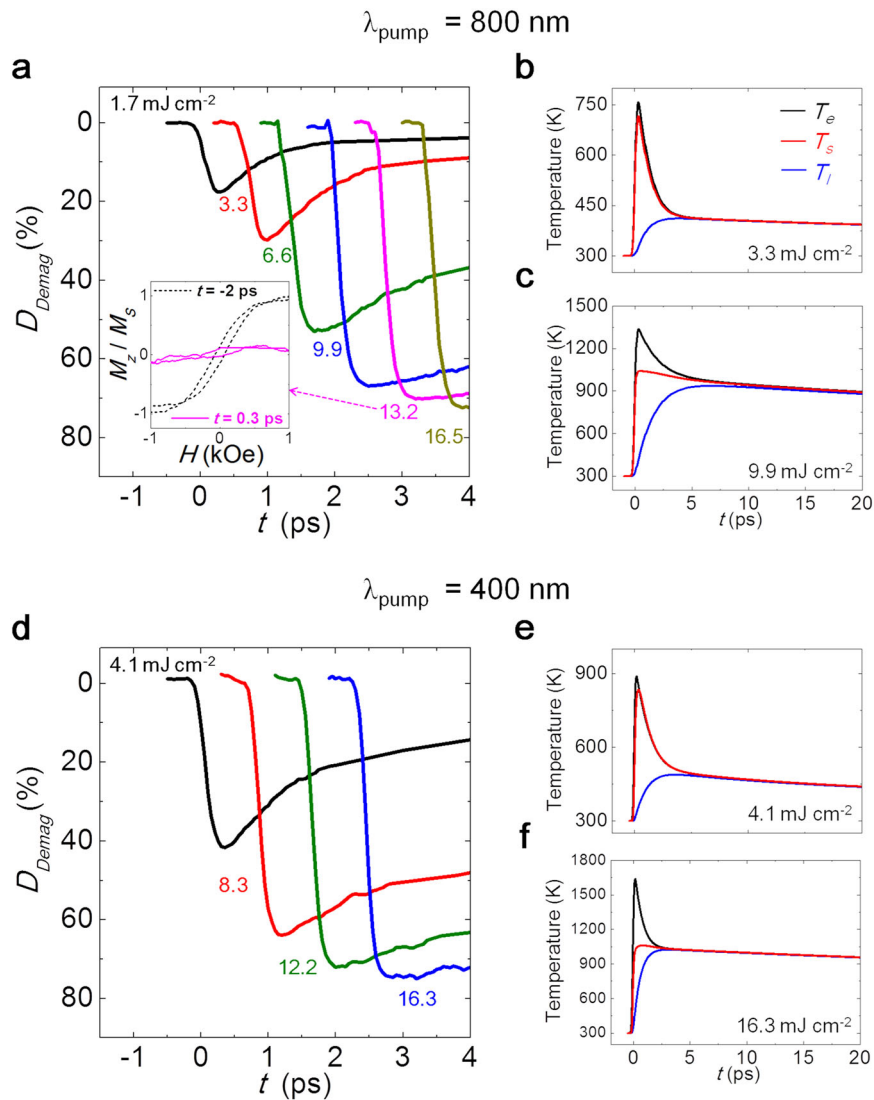
Fig. 2 Temporal change of the degree of demagnetization (D_{demag}) and temperatures. For the case of wavelength of pump pulse $\lambda_{pump} = 800$ nm, **a** Time-resolved magneto-optical Kerr effect (TR-MOKE) data measured for $1.7 \leq F_P$ (pump fluence) ≤ 16.5 mJ cm^{-2}; inset: hysteresis loops with probe-beam modulation measured at delay time $t = -2$ ps (dotted line) and 0.3 ps (solid line) at $F_P = 13.2$ mJ cm^{-2}. Spin temperature T_s (red), electron temperature T_e (black), and lattice temperature T_l (blue) during the initial 30 ps for $F_P =$ **b** 3 and **c** 9.9 mJ cm^{-2}. For the case of $\lambda_{pump} = 400$ nm, **d** TR-MOKE data measured for $4.1 \leq F_P \leq 16.3$ mJ cm^{-2}. T_s (red), T_e (black), and T_l (blue) during the initial 30 ps for $F_P =$ **e** 4.1, **f** 16.3 mJ cm^{-2}.

ratio particularly seems to play an important role in determining the energy-excessive spin dynamics on a sub-ps timescale.

Discussion

The previous studies[17,44–46] in static cases have shown that the temperature dependence of A_{ex} is expressed as power of M with a scaling exponent ranging from 1.79 to 1.82 in case of Co. We set the exponent to be 1.8 and write the temporal variance of A_{ex} as

$$A_{ex}[t] = A_{ex0} \times M^{1.8}[T_s[t]]. \tag{5}$$

Based on Eq. (5), time-dependent A_{ex} is plotted in Fig. 4. The increase in F_P results in the reduction of A_{ex}, as generally expected in static cases. However, the recovery of reduced A_{ex} depends sensitively on F_P. A_{ex} decreases asymptotically as F_P increases, and saturates at $F_P \approx 9.9$ mJ cm^{-2} ($\lambda_{pump} = 800$ nm) or 12.1 mJ cm^{-2} ($\lambda_{pump} = 400$ nm) without further decrease with respect to the fluence higher than this value, which is expected from the saturated behavior of the D_{demag} at high F_P. At $F_P > 9.9$ mJ cm^{-2}, A_{ex} was ~1 pJ m^{-1}. The maximal decrease of A_{ex} occurred at $t = 0.3$ ps when the maximum D_{demag} occurs in the TR-MOKE

measurement. TR-MOKE data (Fig. 1a) show a similar trend to the trend in A_{ex} (Fig. 4). The magnetization M and A_{ex} recovered quickly at low F_P whereas the recovery becomes significantly slow for high F_P.

It should be noted that Eq. (5) is valid for the steady-state case and we use the very rough assumption that considering that even in the out-of-equilibrium case, there could be a rough relation between A_{ex} and temperature-dependent M[9]. Indeed, although we use 3TM[23,28,29], 3 temperatures are not fundamentally well defined in the out-of-equilibrium state and only phenomenologically defined once 3TM is used. On the other hand, we consider that the $M[T]$ might not be totally different compared to the steady-state case, since the estimated spin temperature is still below T_C. The pump pulse excites the electrons around the Fermi energy so that the excited electrons occupy the allowed energy levels above the Fermi energy, while remaining electrons still follow the Fermi-Dirac distribution. Moreover, the thermal equilibrium among 3 temperatures is achieved around ~10 ps and thus, the $M[T]$ will be soon replaced back to the equilibrium case after this timescale. Therefore, we think that there might be a
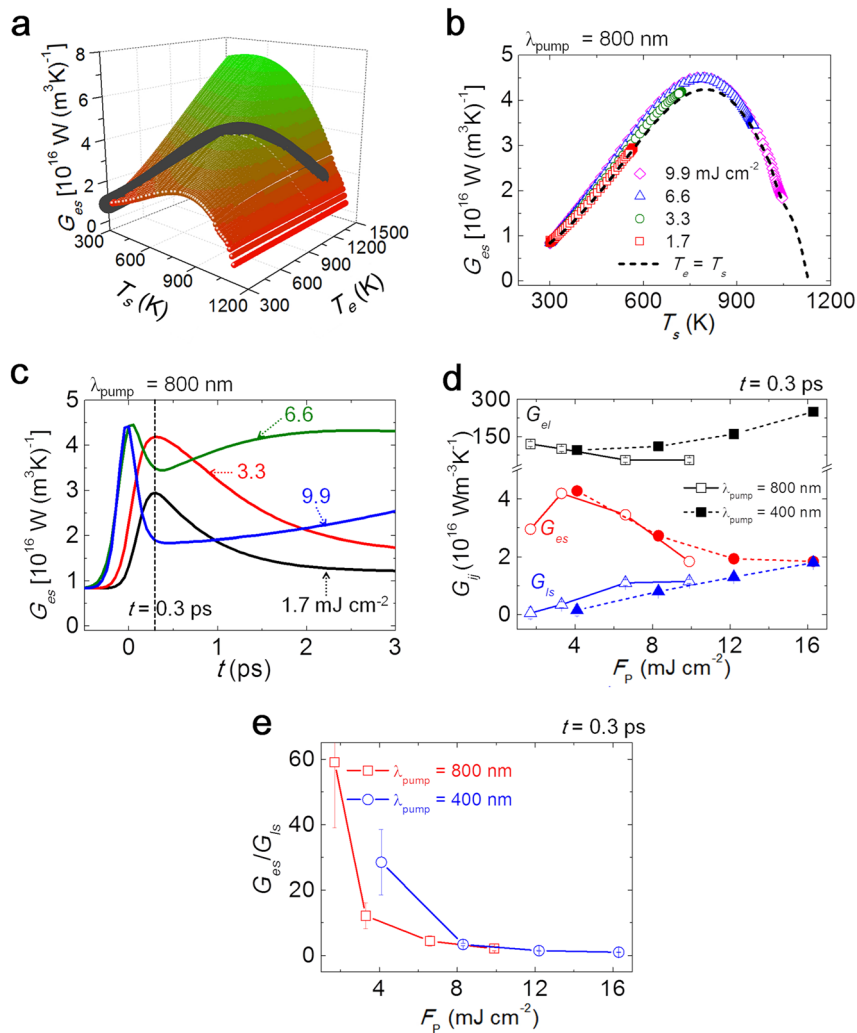
Fig. 3 Temporal change of interaction channels [G_{es} (electron-spin interactio channel), G_{el} (electron-lattice interactio channel), and G_{ls} (lattice-spin interactio channel)] and the exchange stiffness. a 3D map of G_{es} vs T_s (spin temperature) and T_e (electron temperature). Dark gray line: trajectory of G_{es} at 9.9 mJ cm^{-2} for -1 to 0.3 ps. **b** G_{es} vs T_s for -1 to 0.3 ps at $1.7 \leq F_P$ (pump fluence) ≤ 9.9 mJ cm^{-2} (wavelength of pump pulse $\lambda_{pump} = 800$ nm). Black dashed line: $T_e = T_s$. **c** G_{es} vs. the delay time (t) between -1 to 3 ps at $1.7 \leq F_P \leq 9.9$ mJ cm^{-2} ($\lambda_{pump} = 800$ nm). Vertical dashed line: $t = 0.3$ ps. **d** Interaction channels (G_{es}, G_{el}, and G_{ls}) vs F_P at $t = 0.3$ ps for the case of 800 and 400-nm λ_{pump}. Error bars represent that lowest standard error region (<5%) during each fitting parameter by G-3TM. G_{es} is not fitting paramert in G-3TM. **e** G_{es}/G_{ls} vs F_P at $t = 0.3$ ps for the case of 800 and 400-nm λ_{pump}. Error bars represent that lowest standard error region (<5%) during each fitting parameter by G-3TM.
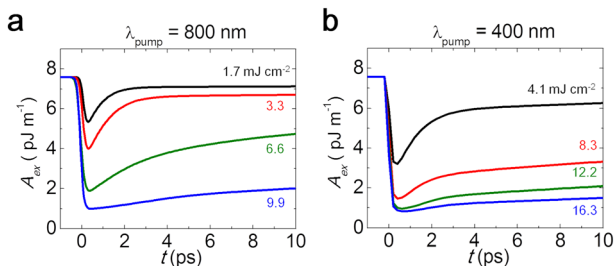

Fig. 4 Temporal profile of exchange stiffness A_{ex} for various fluence. a wavelength of pump pulse $\lambda_{pump} = 800$ nm. **b** $\lambda_{pump} = 400$ nm.

deviation of $M[T]$ from the steady-state case, but the $M[T]$ can be roughly approximated based on the Eq. (5). We have varied the exponent value from 1.6 to 2.0 in our analysis, where no significant difference in the analysis result is observed.

Possible mechanisms of A_{ex} reduction might be involved with Stoner exchange splitting reduction[9], where it has been reported that dynamic exchange splitting is determined by time-dependent magnetization $M(t)$. On the other hand, magnon generation should be also an important factor[47], where it has been reported that the magnon contribution to demagnetization is dominant only on a very short (700 fs) timescale. Thus, in our case, we consider that the magnon contribution could exist on a sub-ps timescale, while the Stoner exchange splitting reduction is lasting longer up to few tens of ps since there is still a substantial amount of demagnetized $M(t)$ in the present work. It should be also noted that G-3TM, which our whole analysis is based on, includes the magnon generation by hot electron as a key mechanism in the model. In G-3TM, electron-spin interaction Hamiltonian intrinsically deals with the effect of magnon generation, which might be reflected in the A_{ex} dynamics, particularly on the sub-ps timescale. The effective Stoner exchange splitting reduction is understood based on the reduced $M(t)$ over the whole process of demagnetization and remagnetization. It should be mentioned that our film is prepared on a Si substrate with no doping, which can be approximated to be an insulator so that the spin diffusion effect could be negligible in the process of demagnetization.
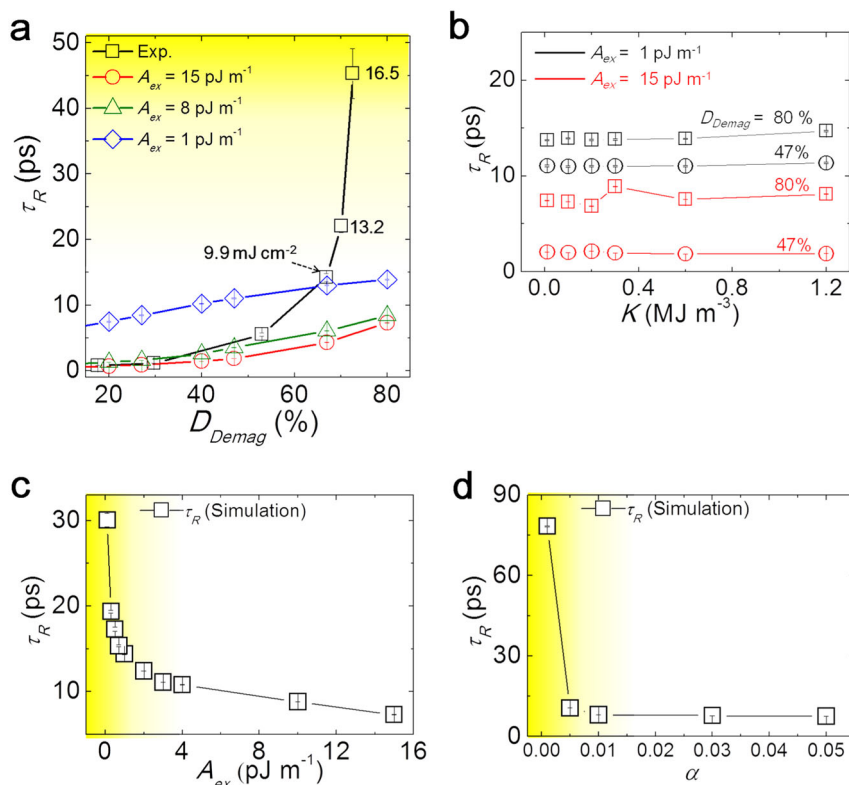
Fig. 5 Micromagnetic simulation. a τ_R (Remagnetization time) vs. D_{demag} (degree of demagnetization). Experimental data (black open squares) together with simulation results for different exchange stiffness A_{ex} of 15 (red), 8 (green), and 1 (blue) pJ m^{-1}. The corresponding values of the pump fluence are written next to the experimental data points. Yellow region: $F_P > 9.9$ mJ cm^{-2} where τ_R is abruptly increased. **b** τ_R vs. K (magnetic anisotropy) for D_{demag} of 47 (circle) and 80 % (square). A_{ex} is changed from 1 (black) to 15 (red) pJ m^{-1}. **c** Simulated result of τ_R vs. A_{ex}. The D_{demag} is fixed to be 80 %. Yellow region corresponds to the yellow region in **b**. **d** Simulated result of τ_R vs. α (Gilbert damping constant). All error bars represent standard error of the single exponential fitting.

The above analysis reveals that the significant increase of the remagnetization time (τ_R) (Fig. 1b) for high fluence is directly related to the reduction of A_{ex}. In order to confirm how much A_{ex} or demagnetization state affects the remagnetization process, we have carried out another series of independent micromagnetic simulations. The micromagnetic simulation was performed using the Object-Oriented Micromagnetic Framework[48] based on the Landau-Lifshitz-Gilbert (LLG) equation:

$$\frac{dM[\vec{r},t]}{dt} = -\gamma(M[\vec{r},t] \times H_{\text{eff}}[\vec{r},t]) + \frac{\gamma\alpha}{M_s}\{M[\vec{r},t] \times (M[\vec{r},t] \times H_{\text{eff}}[\vec{r},t])\}. \quad (6)$$

where the gyromagnetic ratio $\gamma = 2.210 \times 10^5$ m (A s)$^{-1}$ and H_{eff} is the effective magnetic field. Since the micromagnetic simulation does not consider the temperature variation, it is not suitable to dynamics study but still provides valuable information about the material properties for remagnetization at a fixed temperature. We set the initial degree of magnetization according to the measurement and simulated how the remagnetization proceeds for different magnetic parameters such as A_{ex} and magnetic anisotropy. In the simulations, an external magnetic field of 1.7 kOe was applied with an angle of 0° to the surface normal of the film as in the experiments. The saturation magnetization M_s of the film was set as 10^3 kA m^{-1}. Magnetic anisotropy constant K was set as 6×10^5 J m^{-3}. Gilbert damping constant α was set as 0.05. The cell size was $0.5 \times 0.5 \times 0.5$ nm^3 and the sample size was $50 \times 50 \times 7.5$ nm^3. The initial demagnetization state is set by the experimentally-measured D_{demag} for various F_P (Fig. 1b is re-plotted with respect to D_{demag} corresponding to various F_P (black open squares) as shown in Fig. 5a). As the D_{demag} increases, τ_R

increases, drastically at larger D_{demag} than 60 %. To determine parameters that are most responsible for the abrupt increase of τ_R with the increase of F_P (or high D_{demag}), we performed micromagnetic simulations for $A_{ex} = 1$, 8, and 15 pJ m^{-1}. In each simulation, A_{ex} was fixed throughout the simulation. Simulations with $A_{ex} = 8$ (Fig. 5a, green triangle) and 15 pJ m^{-1} (Fig. 5a, red circle) agree well with experiments at low F_P (or low D_{demag}). The literature value[40,41] of A_{ex} of Co/Pt multilayer for a static case is ~ 10 pJ m^{-1}, which is consistent with the range of our simulation parameter. In the simulation with $A_{ex} = 1$ pJ m^{-1}, τ_R was substantially higher than the experimental observations (low D_{demag}).

Magnetic anisotropy is another important parameter that might affect τ_R. The magnetic anisotropy is determined mostly by the crystal structure, sample shape, and multilayer interfaces. This anisotropy produces a perpendicular magnetic anisotropy in the Co/Pt multilayer used in the present study. The micromagnetic simulation of τ_R for various magnetic anisotropy constants K for various D_{demag} from 47 to 80 % showed no significant change of τ_R at $0.01 \leq K \leq 1.2$ MJ m^{-3} (Fig. 5b). The measured value of K for the Co/Pt multilayer in the present study is $K = 0.6$ MJ m^{-3}, which is within our simulation range. Thus, we infer that the variation in K is not responsible for the increase of τ_R. This independence is expected because the variation of K will mostly affect the total effective field without directly modifying spin-spin or spin-electron interactions.

We also systematically changed A_{ex} in micromagnetic simulations with the D_{demag} being fixed at 80% (Fig. 5c). As A_{ex} was varied from 4.0 to 0.1 pJ m^{-1}, τ_R increased from 10.8 to 30.1 ps. In particular, at $A_{ex} < 1$ pJ m^{-1}, τ_R increases rapidly in a similar manner to the experimental observation (near high F_P in Fig. 1b,

or near high D_{demag} in Fig. 5a). The increase in F_P can be expected to reduce A_{ex} significantly, resulting in a large increase of τ_R. The decrease in A_{ex} is generally expected to cause the increase in τ_R, because the reduced spin-spin interaction weakens the ordering among neighboring spins. This micromagnetic simulation also confirms the analysis by G-3TM.

We have carried out a simulation with the variation of damping parameter (α), as seen in Fig. 5d. A_{ex} is set to be 11 pJ m^{-1}, anisotropy constant K is 0.6 MJ m^{-3}, and D_{demag} is set to be 80%. τ_R is found to be insensitive if α is larger than 0.005, as seen in the figure. For α smaller than 0.005, τ_R drastically increases due to the significant contribution of precessional oscillation. α of Co/Pt multilayer is reported in the range of 0.02–0.1[49,50], which is much larger than 0.005.

In summary, we have investigated the dynamical variation of A_{ex} on an ultrafast timescale, by TR-MOKE and reflectivity measurements in a Co/Pt multilayer for various F_P. Our phenomenological analysis suggests that the ultrafast remagnetization mechanisms may be governed by the dynamically changing A_{ex}, which is also closely related to G_{es}, and G_{ls} also becomes non-negligible in case of high F_P. Our comprehensive micromagnetic simulations implies that significantly reduced A_{ex} is responsible for the large remagnetization time. These results demonstrate the possibility of engineering magnetic properties on an ultrafast timescale by modifying G_{es}, G_{ls}, and G_{el}.

Methods

MOKE measurement. TR-MOKE measurements with a pump-probe stroboscope were performed on a Co/Pt multilayer. We used the femtosecond laser pulses generated by a Ti:sapphire multipass amplifier operating at a repetition rate of 3 kHz with a center wavelength of 800 nm and a pulse duration of 25 fs. We employed two pump wavelengths of 800 nm and 400 nm obtained from BBO (BaB$_2$O$_4$) crystal. As probe pulses, one wavelength of 800 nm was used. F_P was varied from 1.7 to 28.5 mJ cm^{-2} and probe fluence was 0.3 mJ cm^{-2}. For TR-MOKE measurements, the pump beam was modulated using a mechanical chopper at 500 Hz. An external magnetic field of 1.7 kOe was applied throughout the measurements, with an angle of 0° to the surface normal of the film to keep the initial sample condition saturated before a subsequent pump pulse.

To estimate the D_{demag}, we conducted a series of hysteresis measurements at times of $t = -2$ ps and 0.3 ps under the same TR-MOKE setup with only probe-beam modulation at 500 Hz, while sweeping a magnetic field from -1.7 kOe to 1.7 kOe. The hysteresis measurement at $t = -2$ ps gives the magnetization of an intact sample.

Sample. [Co(6.2 Å)/Pt(7.7 Å)]$_5$ multilayer films were deposited on Si substrates by dc magnetron sputtering, then capped by a 22-Å Pt layer to prevent the oxidation of the surface. The structure of the Co/Pt multilayers with well-defined interfaces was confirmed by a low angle X-ray diffraction and extended X-ray absorption fine structure analysis. The film had a perpendicular magnetic anisotropy ($K = 0.63$ MJ m^{-3}) and saturation magnetization ($M_s = 1.04 \times 10^3$ kA m^{-1}), which are similar to literature values[24–27].

Data availability

The data that support the findings of this study are available from the corresponding author upon reasonable request.

Code availability

The source codes used for G-3TM fitting/micromagnetic simulation are available from the corresponding author upon reasonable request.

References

1. Kittel, C. Physical theory of ferromagnetic domains. *Rev. Mod. Phys.* **21**, 541–583 (1949).
2. Anderson, P. W. Generalizations of the Weiss molecular field theory of antiferromagnetism. *Phys. Rev.* **79**, 705 (1950).
3. Zakeri, K. et al. Direct probing of the exchange interaction at buried interfaces. *Nat. Nanotechnol.* **8**, 853–858 (2013).
4. Zener, C. Interaction between the d-Shells in the Transition. *Met. Phy. Rev.* **81**, 440 (1951).
5. Yan, B. et al. Observation of dipolar spin-exchange interactions with lattice confined polar molecules. *Nature* **501**, 521–525 (2013).
6. Dzyaloshinskii, I. Ie dzyaloshinskii. *Sov. Phys. JETP* **5**, 1259 (1957).
7. Yang, H., Thiaville, A., Rohart, S., Fert, A. & Chshiev, M. Anatomy of Dzyaloshinskii–Moriya interaction at Co/Pt interfaces. *Phys. Rev. Lett.* **115**, 267210 (2015).
8. Moriya, T. Anisotropic superexchange interaction and weak ferromagnetism. *Phys. Rev.* **120**, 91–98 (1960).
9. Mueller, B. Y. et al. Feedback effect during ultrafast demagnetization dynamics in ferromagnets. *Phys. Rev. Lett.* **111**, 167204 (2013).
10. Rhie, H.-S., Dürr, H. A. & Eberhardt, W. Femtosecond electron and spin dynamics in Ni/W(110) films. *Phys. Rev. Lett.* **90**, 247201 (2003).
11. Zhang, G. P., Bai, Y. H. & George, T. F. Ultrafast reduction of exchange splitting in ferromagnetic nickel. *J. Phys. Condens. Matter* **28**, 236004 (2016).
12. Jain, S. et al. From chaos to selective ordering of vortex cores in interacting mesomagnets. *Nat. Commun.* **3**, 1330 (2012).
13. Wintz, S. et al. Magnetic vortex cores as tunable spin-wave emitters. *Nat. Nanotech.* **11**, 948–953 (2016).
14. Zhang, X., Zhou, Y. & Ezawa, M. Magnetic bilayer-skyrmions without skyrmion Hall effect. *Nat. Commun.* **7**, 10293 (2016).
15. Nagaosa, N. & Tokura, Y. Topological properties and dynamics of magnetic skyrmions. *Nat. Nanotech.* **8**, 899–911 (2013).
16. Atxitia, U. et al. Multiscale modeling of magnetic materials: temperature dependence of the exchange stiffness. *Phy. Rev. B* **82**, 134440 (2010).
17. Moreno, R. et al. Temperature-dependent exchange stiffness and domain wall width in Co. *Phy. Rev. B* **94**, 104433 (2016).
18. Mathias, S. et al. Probing the timescale of the exchange interaction in a ferromagnetic alloy. *Proc. Natl Acad. Sci. USA* **109**, 4792–4797 (2012).
19. Batignani, G. et al. Probing ultrafast photo-induced dynamics of the exchange energy in a Heisenberg antiferromagnet. *Nat. Photon.* **9**, 506–510 (2015).
20. Zhang, G. P., Gu, M. & Wu, X. S. Ultrafast reduction in exchange interaction by a laser pulse: alternative path to femtomagnetism. *J. Phys. Cond. Matter* **26**, 376001 (2014).
21. Mentink, J. H., Balzer, K. & Eckstein, M. Ultrafast and reversible control of the exchange interaction in Mott insulators. *Nat. Commun.* **6**, 6708 (2015).
22. Mikhaylovskiy, R. V. et al. Ultrafast optical modification of exchange interactions in iron oxides. *Nat. Commun.* **6**, 8190 (2015).
23. Manchon, A., Li, Q., Xu, L. & Zhang, S. Theory of laser-induced demagnetization at high temperatures. *Phy. Rev. B* **85**, 064408 (2012).
24. Zeper, W. B., Greidanus, F. J. A. M., Carcia, P. F. & Fincher, C. R. Perpendicular magnetic anisotropy and magneto optical Kerr effect of vapor deposited Co/Pt-layered structures. *J. Appl. Phys.* **65**, 4971 (1989).
25. Davies, J. E. et al. Magnetization reversal of Co/Pt multilayers: microscopic origin of high-field magnetic irreversibility. *Phys. Rev. B* **70**, 224434 (2004).
26. San Emeterio Alvarez, L. et al. Spin-transfer-torque-assisted domain-wall creep in a Co/Pt multilayer wire. *Phys. Rev. Lett.* **104**, 137205 (2010).
27. Quach, D.-T. et al. Minor hysteresis patterns with a rounded/sharpened reversing behavior in ferromagnetic multilayer. *Sci. Rep.* **8**, 4461 (2018).
28. Shim, J.-H. et al. Ultrafast giant magnetic cooling effect in ferromagnetic Co/Pt multilayers. *Nat. Comm.* **8**, 796 (2017).
29. Beaurepaire, E., Merle, J.-C., Daunois, A. & Bigot, J.-Y. Ultrafast spin dynamics in ferromagnetic nickel. *Phys. Rev. Lett.* **76**, 4250 (1996).
30. Lu, G., Wang, X. D., Duan, Y. Y. & Li, X. W. Effects of non-ideal structures and high temperatures on the insulation properties of aerogel-based composite materials. *J. Non-Cryst. Sol.* **357**, 3822 (2011).
31. Bagayoko, D. et al. Band structure of bcc cobalt. *Phys. Rev. B* **27**, 7046 (1983).
32. Sun, C.-K., Vallée, F., Acioli, L. H., Ippen, E. P. & Fujimoto, J. G. Femtosecondtunable measurement of electron thermalization in gold. *Phys. Rev. B* **50**, 15337–15348 (1994).
33. Kruglyak, V., Hicken, R., Matousek, P. & Towrie, M. Spectroscopic study of optically induced ultrafast electron dynamics in gold. *Phys. Rev. B* **75**, 035410 (2007).
34. Kimling, J. et al. Ultrafast demagnetization of FePt:Cu thin films and the role of heat capacity. *Phys. Rev. B* **90**, 224408 (2014).
35. Iihama, S. et al. Ultrafast demagnetization of L10 FePt and FePd ordered alloys. *J. Phys. D. Appl. Phys.* **49**, 035002 (2016).
36. Atxitia, U., Chubykalo-Fesenko, O., Walowski, J., Mann, A. & Münzenberg, M. Evidence for thermal mechanisms in laser-induced femtosecond spin dynamics. *Phys. Rev. B* **81**, 174401 (2010).
37. Roth, T. et al. Temperature dependence of laser-induced demagnetization in Ni: a key for understanding the underlying mechanism. *Phys. Rev. X* **2**, 021006 (2012).
38. Kuiper, K. C. et al. Spin-orbit enhanced demagnetization rate in Co/Pt-multilayers. *Appl. Phys. Lett.* **105**, 202402 (2014).

39. Stamm, C., Pontius, N., Kachel, T., Wietstruk, M. & Dürr, H. A. Femtosecond x-ray absorption spectroscopy of spin and orbital angular momentum in photoexcited Ni films during ultrafast demagnetization. *Phy. Rev. B* **81**, 104425 (2010).

40. Eimüller, T. et al. Spin-reorientation transition in Co/Pt multilayers on nanospheres. *Phys. Rev. B* **77**, 134415 (2008).

41. Okamoto, S., Kikuchi, N., Furuta, M., Kitakami, O. & Shimatsu, T. Switching behaviors and its dynamics of a Co/Pt nanodot under the assistance of rf fields. *Phys. Rev. Lett.* **109**, 237209 (2012).

42. Koopmans, B. et al. Explaining the paradoxical diversity of ultrafast laser-induced demagnetization. *Nat. Mater.* **9**, 259–265 (2010).

43. Atxitia, U. & Chubykalo-Fesenko, O. Ultrafast magnetization dynamics rates within the Landau-Lifshitz-Bloch model. *Phys. Rev. B* **84**, 144414 (2011).

44. Turek, I., Kudrnovsky, J., Drchal, V., Bruno, P. & Blügel, S. Ab initio theory of exchange interactions in itinerant magnets. *Phys. Status Solidi (b)* **236**, 318 (2003).

45. Pajda, M., Kudrnovský, J., Turek, I., Drchal, V. & Bruno, P. Ab initio calculations of exchange interactions, spin-wave stiffness constants, and Curie temperatures of Fe, Co, and Ni. *Phys. Rev. B* **64**, 174402 (2001).

46. Kvashnin, Y. O., Sun, W., Marco, I. D. & Eriksson, O. Electronic topological transition and noncollinear magnetism in compressed hcp Co. *Phys. Rev. B* **92**, 134422 (2015).

47. Turgut, E. et al. Stoner versus Heisenberg: ultrafast exchange reduction and magnon generation during laser-induced demagnetization. *Phys. Rev. B* **94**, 220408 (2016).

48. Donahue, M. J. & Porter, D. G. OOMMF User's Guide. http://math.nist.gov/oommf (2002).

49. Fujita, N. et al. Damping constant of Co/Pt multilayer thin-film media. *J. Magn. Magn. Mater.* **320**, 3019–3022 (2008).

50. Barman, A. et al. Ultrafast magnetization dynamics in high perpendicular anisotropy [Co/Pt]$_n$ multilayers. *J. Appl. Phys.* **101**, 09D102 (2007).

Author contributions

J.-H.S., A.A.S, Y.S., J.-W.K., H.-G.P. and S.-H.L. collected data and performed all the analyses; K.M.L. and J.R.J. fabricated the samples; D.E.K. and D.-H.K. were involved in study design. All authors discussed the results and commented on the manuscript.

Competing interests

The authors declare no competing interests.

Additional information

Supplementary information is available for this paper at https://doi.org/10.1038/s42005-020-0346-y.

Correspondence and requests for materials should be addressed to D.-H.K. or D.E.K.

Reprints and permission information is available at http://www.nature.com/reprints

Publisher's note Springer Nature remains neutral with regard to jurisdictional claims in published maps and institutional affiliations.